

● Original Contribution

A CLOSED-FORM DIFFERENTIAL FORMULATION FOR ULTRASOUND SPATIAL CALIBRATION: SINGLE WALL PHANTOM

MOHAMMAD NAJAFI,* NARGES AFHAM,* PURANG ABOLMAESUMI,* and ROBERT ROHLING*[†]

*Department of Electrical and Computer Engineering, University of British Columbia, Vancouver, British Columbia, Canada; and [†]Department of Mechanical Engineering, University of British Columbia, Vancouver, British Columbia, Canada

(Received 23 May 2014; revised 17 October 2014; in final form 25 November 2014)

Abstract—Calibration is essential in freehand 3-D ultrasound to find the spatial transformation from the image coordinates to the sensor coordinate system. Ease of use, simplicity, precision and accuracy are among the most important factors in ultrasound calibration, especially when aiming to make calibration more reliable for day-to-day clinical use. We introduce a new mathematical framework for the simple and popular single-wall calibration phantom with a plane equation pre-determination step and the use of differential measurements to obtain accurate measurements. The proposed method provides a novel solution for ultrasound calibration that is accurate and easy to perform. This method is applicable to both radiofrequency (RF) and B-mode data, and both linear and curvilinear transducers. For a linear L14-5 transducer, the point reconstruction accuracy (PRA) of reconstructing 370 points is 0.73 ± 0.23 mm using 100 RF images, whereas the triple N-wire PRA is 0.67 ± 0.20 mm using 100 B-mode images. For a curvilinear C5-2 transducer, the PRA using the proposed method is 0.86 ± 0.28 mm on 400 points using 100 RF images, whereas N-wire calibration gives a PRA of 0.80 ± 0.46 mm using 100 B-mode images. Therefore, the accuracy of the proposed variation of the single-wall method using RF data is practically similar to the N-wire method while offering a simpler phantom with no need for accurate design and construction. (E-mail: rohling@ece.ubc.ca) © 2015 World Federation for Ultrasound in Medicine & Biology.

Key Words: Ultrasound, Calibration, Closed form, Single wall, Differential.

INTRODUCTION

Ultrasound is a tolerable, portable, inexpensive and real-time modality that can produce 2-D and 3-D images, and therefore, it is a valuable intra-operative imaging modality to guide surgeons aiming to achieve higher accuracy in the intervention and improve patient outcomes. Specifically, there has been a surge of interest in integrating ultrasound imaging into a number of clinical procedures, such as laparoscopic procedures (Nakamoto et al. 2008), minimally invasive cardiac surgeries and therapies (Huang et al. 2010), spinal fusion surgeries (Yan et al. 2011), orthopedic surgeries (Paulius et al. 2008; Peters et al. 2010), guidance for breast biopsy (Cosio et al. 2010), tumor resection (Krekel et al. 2011), brain neurosurgery (Unsgård, 2009) and radiation therapy (Chinnaiyan et al. 2003).

In many such clinical procedures, there is a benefit in tracking the spatial location of the transducer while sweeping over the anatomy of interest. This “freehand” 3-D ultrasound imaging approach can be used for visualization and quantitative measurements such as 3-D locations, sizes and volumes of anatomic structures. Also, by tracking an ultrasound transducer, multiple ultrasound data sets can be mapped into the same coordinate system to construct larger volumes with an extended field of view. Ultrasound with positional information also facilitates registration to complementary image modalities such as magnetic resonance imaging (Melvær et al. 2012). In some applications, laparoscopic, biopsy and surgical tools are also tracked, and their positions should be converted to a common coordinate system as the ultrasound images. Augmented reality is yet another application that can benefit from tracked ultrasound transducers.

The accuracy of freehand-tracked ultrasound is an important factor in the overall accuracy of the aforementioned procedures (Peterhans et al. 2010). In many cases, high accuracy results in numerous clinical benefits. For example, intra-operative ultrasound imaging of the vertebrae, combined with automated registration to

Address correspondence to: Robert Rohling, Department of Electrical and Computer Engineering, University of British Columbia, 3059-2332 Main Mall, Vancouver, BC, V6T 1Z4, Canada. E-mail: rohling@ece.ubc.ca

pre-operative computed tomography, could improve spine surgery by improving accuracy, reducing operative time and decreasing invasiveness. The resulting benefits include lower surgical risk, increased possibility of performing more complex instrumentation, decreased post-operative complications, more confidence in the surgical procedures and better post-operative function (Yan et al. 2011). In performing neuronavigation based on intra-operative 3-D ultrasound, precise surgical planning and intervention are possible, resulting in the reduction of residual tumor volumes, reduced operation times and better patient outcomes (Lindseth et al. 2002). In ultrasound-guided liver tumor resection, the surgeon relies on ultrasound volumes for accurate orientation with respect to the tumor. High accuracy is needed to provide tumor-free resection margins and to preserve vessels close to the tumor (Gulati et al. 2009). For a breast tumor biopsy, the needle tip should be accurately located inside several positions of the tumor (Cosio et al. 2010). In real-time visualization of high-intensity focused ultrasound for prostate cancer treatment with 3-D ultrasound, precise knowledge of the size and location of the tumor and the treated areas can improve the outcome (Rouvire et al. 2007).

In all the clinical applications that use freehand-tracked ultrasound to reconstruct 3-D ultrasound volumes, such as those examples cited above, the challenge is to precisely locate the ultrasound image pixels with respect to a tracking sensor on the transducer. In a process called spatial calibration, the spatial transformation between the ultrasound image coordinates and the transducer's coordinate system is determined.

Many methods have been proposed for ultrasound calibration over the last two decades. Most methods are based on imaging an artificial object with known geometric parameters called a phantom. To calculate the calibration parameters, the phantom geometry, the ultrasound image features and usually a mathematical model are used. Calibration methods can thus be categorized according to the phantom shape.

Point-based phantoms can be constructed as a bead (Amin et al. 2001; Detmer et al. 1994), crossed-wires (Melvær et al. 2012; Trobaugh et al. 1994; Yaniv et al. 2011) or the center of a sphere (Brendel et al. 2004). Wire-based phantoms usually have N- or Z-shaped patterns, but other configurations can also be used (Boctor et al. 2004; Chen et al. 2009; Hsu et al. 2008b; Pagoulatos et al. 2001; Peterhans et al. 2010). The method of Chen et al. (2009) is used in the open-source PLUS ultrasound software employed by several research groups (Lasso et al. 2012). In plane-based methods, the phantom can be a fixed plane, as in the single-wall method (Najafi et al. 2012b; Prager et al. 1998; Yaniv et al. 2011) or its variant the Cambridge phantom (Prager et al. 1998), or multiple planes (Najafi et al.

2012a). Another approach is based on registration of 2-D ultrasound images with the 3-D model of the phantom (Bergmeir et al. 2009; Blackall et al. 2000; Lange et al. 2011). Some calibration methods do not require a phantom and use a calibrated stylus (Hsu et al. 2008a; Khamene and Sauer 2005; Muratore and Galloway 2001) or use changes in speckle from transducer movements (Boctor et al. 2006).

Calibration methods can also be categorized according to their mathematical solution technique. Some of the calibration methods solve the calibration parameters by iteratively minimizing a cost function based on the mathematical geometry of the problem (Detmer et al. 1994; Melvær et al. 2012; Prager et al. 1998). Iterative methods are subject to suboptimal local minima and are sensitive to initial estimates; therefore, they are less robust in general than closed-form solutions (Eggert et al. 1997). Some methods use a closed-form solution derived from the geometry of the phantom to determine calibration parameters (Boctor et al. 2004; Chen et al. 2009; Najafi et al. 2012b). Not all methods use a mathematical solver to calculate calibration parameters. For example, there are methods that are based on iterative manual alignment of the ultrasound image with a thin planar phantom (Gee et al. 2005; Lindseth et al. 2003). Detailed reviews, comparison of different calibration methods and a summary of various validation techniques can be found in survey papers (Hsu et al. 2009; Mercier et al. 2005).

Ease of use, simplicity, precision (repeatability) and accuracy are among the most important factors in ultrasound calibration, especially when the aim is to make calibration more reliable for day-to-day clinical use. Phantoms that must be built with a specific geometry, or from specific material, or with a specific scanning or alignment protocol or phantoms that use complicated segmentation or registration algorithms are barriers to simplicity and ease of use for a user. The single-wall method uses perhaps the simplest phantom among other calibration methods. It merely requires a planar object such as the flat bottom surface of the water tank. Such a phantom is part of the popular Stradwin freehand ultrasound system freely available and used by many research groups (Prager et al. 1999).

One of the most important limiting factors in increasing the accuracy of calibration is accurate, absolute localization of phantom features in ultrasound images (Lange et al. 2011). One reason for this is the blurry appearance of features resulting from the finite resolution of the ultrasound images and the presence of noise. Moreover, image formation errors arise from speed of sound variations, refraction and a finite beam width, all of which contribute to distortions in the shape of the depicted features.

Absolute localization of features is even more challenging in point-based and wire-based methods compared with plane-based methods. It is very difficult to accurately localize the actual intersection point of a wire or a point target in an ultrasound image. The reason is that the finite resolution of the ultrasound image and imaging artifacts cause small point-shaped objects to appear as short blurred lines in ultrasound images (Chen *et al.* 2009), and therefore, they do not appear in the shape of a circle, but rather as an asymmetric cloud with a width of several pixels. The finite beam width also affects the accuracy of feature localization of planar objects (Prager *et al.* 1998). A plane appears in the ultrasound image as a line with a thickness related to the beam width and plane orientation. Unlike point features, the *appearance/shape* of the line remains unchanged along the line as long as the plane's inclination relative to the beam direction is not high.

To improve accuracy, the need for absolute localization of the calibration phantom features should be reduced. Therefore in this work, we propose use of the differential measurements of the relative distance between two image features. Advances in differential measurements for ultrasound motion tracking in recent years enable accurate measurements of the relative locations of phantom features. This accuracy can be as high as a few microns when radiofrequency (RF) ultrasound data are used (Walker and Trahey 1995).

The differential measurement can be especially accurate when the shapes of the features are very similar. Because the appearance of a wire varies with depth in the image (Chen *et al.* 2009), it is more difficult to perform accurate measurements of the distance difference of point features unless only pairs of features with similar shapes are selected. Planar phantoms, on the other hand, are ideal because the plane appears as a line with uniform thickness. In fact, echo RF pulses in all RF scan lines exhibit a similar pattern because they all experience the same physics of reflection except for a variation in the ultrasound focus (and, therefore, beam width), which slightly varies with the depth. The relative axial distance of line features can be measured as the relative shift between echo RF pulses and is therefore a differential measurement. This measurement can be performed very accurately, especially with RF data. Redundancy of measurements, because of the presence of many scan lines, is another advantage of planar objects over wires. Redundancy allows averaging of measurements, which can also reduce error from measurement noise.

Previously, we developed a closed-form differential formulation based on a multiwedge phantom comprising five planes (Najafi *et al.* 2014). The method achieved very high accuracy using differential measurements on RF data. A 3-D printer was required to precisely manufacture the multiwedge phantom. However, some users without

such manufacturing ability would prefer a calibration method that does not require a special phantom.

The popular single-wall method (Prager *et al.* 1998) is an obvious choice to consider in extending the differential calibration method to improve ease-of-use. The original single-wall method uses an iterative solver to find the calibration parameters as well as the plane equation. In fact, unlike most calibration methods, the wall phantom is not required to be tracked, and the plane's position and orientation parameters are also determined in the solution. Therefore, although the simplicity of the wall phantom is appealing, it is quite a challenge to achieve high accuracy with a small number of images because of the large number of parameters to be solved.

According to Prager *et al.* (1998), the single-wall phantom produced slightly ill-conditioned sets of calibration equations because of the limited range of scanning motions that resulted in clear images of the wall. There was significant uncertainty in the calibration parameters that led to relatively poor point reconstruction precision. Approximately 500 images were used in those experiments (Prager *et al.* 1998). To improve accuracy, the Cambridge phantom (Prager *et al.* 1998) was proposed, which was more accurate but again required a custom apparatus and accurate mounting on the transducer. The technique was also not fully automatic.

In summary, despite the wealth of calibration methods, including the recent introduction of accurate methods using differential measurements on multiple wedges, there is still a need for improved calibration using the simplest and most popular single-wall method. In this article, we propose an improved variation of the single-wall calibration for both linear and curvilinear transducers and for both RF and B-mode input data. The key is to adapt the differential measurement approach to a single wall. We also propose to simplify the calibration problem by explicitly measuring the position of the plane using a stylus and, thus, reduce the number of unknowns and formulate a closed-form solution. The goal is to obtain good accuracy with a relatively small number of images.

In our preliminary work (Najafi *et al.* 2012b), we developed a closed-form differential formulation for the traditional untracked single-wall method for linear transducers. An updated and detailed description of that method can be found in the Appendix. Similar to the traditional single-wall method, the limited range of possible rotations caused that method to be sensitive to measurement error. Therefore, a new “pre-determined single-wall” method is proposed with fewer parameters to solve by ultrasound calibration. We describe the new method and compare it with the traditional single-wall and N-wire calibrations because they are the most commonly used calibration methods according to our review of the literature to date.

METHODS

The single-wall phantom is simply any planar object with a smooth surface. In our experiments, a $15 \times 15 \times 0.5$ -cm aluminum plate was used. A SonixTOUCH ultrasound machine (Ultrasonix Medical, Richmond, BC, Canada) was used for ultrasound imaging. The experiments were performed using both a linear transducer (38-mm L14-5 linear 2-D transducer with 7.2-MHz center frequency, Ultrasonix) and a curvilinear transducer (C5-2 curvilinear 2-D transducer with 3.5-MHz center frequency, 60-mm radius and 56° field of view, Ultrasonix).

An Optotrak Certus optical tracker (Northern Digital, Waterloo, ON, Canada) was used to track the transducer. A set of active markers with a rigid arranged geometry (rigid body) were attached to the transducer to track its pose. The tracker measures the relative transform from an arbitrary coordinate system defined on the rigid body to the tracker's coordinate system.

Before the experiment, the plane's location was pre-determined with the tip of a stylus to determine the plane equation. An NDI (Northern Digital Inc., Waterloo, Ontario, Canada) four-marker digitizing probe was used for this purpose.

The calibration procedure is first summarized briefly and then derived in detail in the subsequent sections. The wall phantom was immersed at the bottom of a water tank. The wall surface was traced with the stylus to pre-determine the plane equation. Then, with the wall phantom fixed, the wall was scanned with the ultrasound transducer from different angles and positions covering all 6° of freedom. The transducer was fixed with a mechanical arm in each position, and the transducer's position was recorded with the tracker to avoid the influence of tracker lag.

Note that the speed of sound depends on the medium and its temperature. The speed of sound assumed by most ultrasound machines is 1540 m/s, which is the average speed of sound in human tissue. For instance, speed of sound for water at room temperature is approximately 1485 m/s (Mercier et al. 2005). For a linear transducer in water, for example, this scales objects by 4% in the axial direction. In the calibration procedure, either the scale factor should be calculated or the water temperature should be set in the ultrasound machine. Another solution is to match the speed of sound in tissue by increasing the water temperature to approximately 50°C or to add glycerol or ethanol to water at room temperature (Mercier et al. 2005).

If the speed of sound in a medium is different from this assumed value, the objects will appear farther or closer, and their shapes might appear distorted.

The image of the wall appears as a straight line in the ultrasound images. By use of the line equation deter-

mined in each ultrasound image and the position of the transducer obtained with the tracker, it is possible to calculate the calibration transform.

The slope of the line can be accurately determined by differential measurements on ultrasound scan lines. Higher accuracy can be achieved with RF data than with B-mode data, although both are feasible. In a linear transducer, the slope can be calculated simply by measuring the relative shift between the echo RF signatures of two scan lines and considering the lateral distance of the two scan lines. For a curvilinear transducer, again the relative shift of echo RF signatures is measured, and the slope is calculated based on the geometry of the transducer (scan line spacing and line angles). Most of the calibration parameters can be calculated using the line slopes. Linear and curvilinear transducer calibration equations are derived separately below.

Line intercepts are used to determine translation parameters. It is not possible to measure line intercepts with differential measurements. Based on the simulations of the problem, the errors in translation parameters are on the same order of the absolute measurement error, which is in the order of the pulse width.

The calibration goal is to find the 6-degree-of-freedom transformation from the image to the transducer coordinate system, ${}^T T_I$. The transformation from the transducer to the reference coordinate system, ${}^R T_T$, is known by the readings from the tracker (Fig. 1).

Linear transducer calibration

An ultrasound image is composed of multiple RF scan lines, each formed by an aperture of ultrasonic

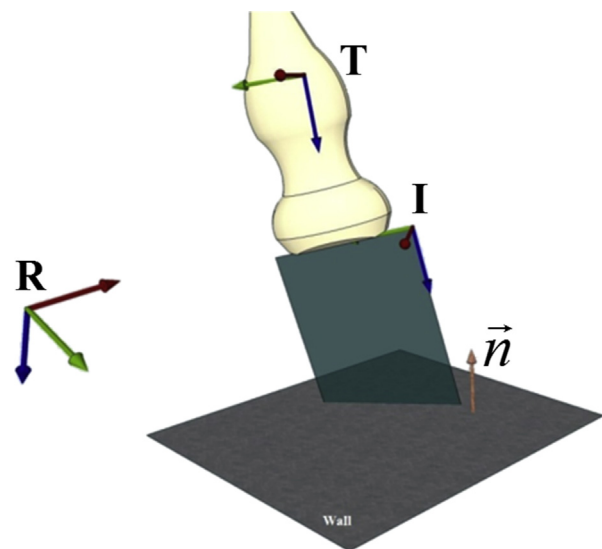


Fig. 1. Calibration setup depicting the coordinate system of the reference (R), transducer (T), ultrasound image (I) and normal (\vec{n}) of a flat plane.

elements. In a linear transducer, all the elements are placed in a linear fashion in the lateral direction, \vec{U} . Also the elements are parallel to each other, and hence the axial vector, \vec{V} , the ultrasound beam propagation direction, is the same for all the RF scan lines (Fig. 2).

The origin of the imaging plane, P_0 , can be assumed, without loss of generality, as the point zero of the first scan line. The lateral pixel-to-millimeter ratio, s_l , is related to the lateral spacing between the elements (assuming equal spacing) and the image line density setting on an ultrasound machine and can be assumed to be known. The axial pixel-to-millimeter ratio, s_a , is related to the speed of sound in the medium and the sampling rate.

Based on this model, the position of each point of the image plane can be described mathematically in 3-D space as

$$P = P_0 + s_l x \vec{U} + s_a y \vec{V}, \quad (1)$$

where x and y are lateral and axial coordinates of the point in the image plane in pixels. To solve for the unknown calibration parameters in the differential scheme, the problem is formulated based on the axial difference of the features in ultrasound scan lines (Fig. 3). The pulse echo reflection of the plane occurs at a certain axial depth, y , for each scan line, x . Considering any two different scan lines, x_i and x_j , in a single image and using (1) yield the equations

$$P_i = P_0 + s_l x_i \vec{U} + s_a y_i \vec{V}, \quad (2)$$

$$P_j = P_0 + s_l x_j \vec{U} + s_a y_j \vec{V}, \quad (3)$$

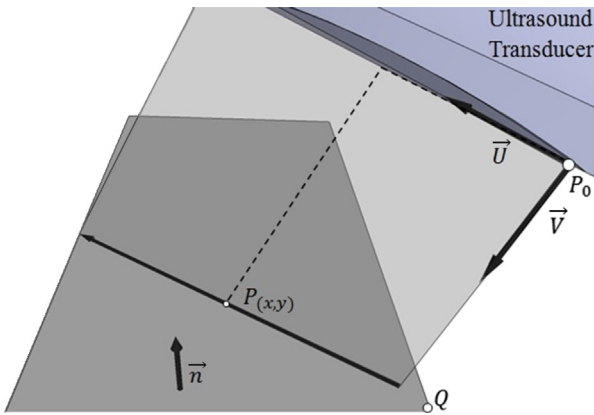


Fig. 2. Intersection of the ultrasound image and the wall plane. \vec{U} is a unit vector in the direction passing through the center of array elements (lateral), and \vec{V} is a unit vector in the direction of the ultrasound beam (axial). P_0 is the origin of the imaging plane. The plane equation is defined with the normal vector, \vec{n} , and a point, Q .

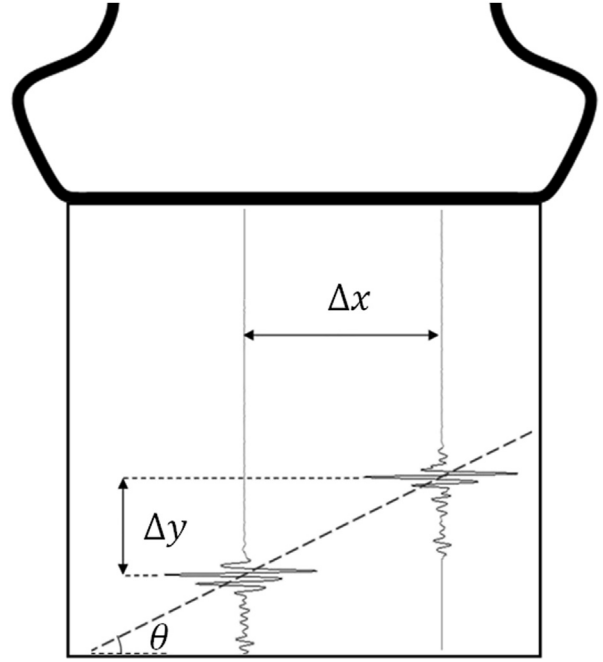


Fig. 3. Differential measurement on two ultrasound scan lines. Line slope is measured with cross-correlation of radiofrequency echoes. $m = \tan(\theta) = \frac{dy}{dx}$.

$$P_i - P_j = s_l (x_i - x_j) \vec{U} + s_a (y_i - y_j) \vec{V}. \quad (4)$$

Since the difference between the two points, $P_i - P_j$, is a vector parallel to the plane, it should be orthogonal to the plane normal vector, \vec{n} . Hence,

$$[s_l (x_i - x_j) \vec{U} + s_a (y_i - y_j) \vec{V}] \cdot \vec{n} = 0, \quad (5)$$

By dividing (5) by $\Delta x = x_i - x_j$ and assuming $\Delta y = y_i - y_j$, $m = \frac{\Delta y}{\Delta x}$ and $k = \frac{s_a}{s_l}$, we have

$$\vec{U} \cdot \vec{n} + km \vec{V} \cdot \vec{n} = 0. \quad (6)$$

In eqn (6), the slope of the line, m , is obtained from the differential measurements by dividing the axial difference by the lateral difference. Lateral difference is, in fact, the distance between scan lines i and j (Fig. 3).

Pre-determined wall method

In this approach, using a stylus, the plane equation of the wall is determined before the experiment. Therefore, plane parameters, \vec{n}_r and Q_r , are now known in the reference coordinate system. All the previous derivations, including parameters in (6), can be defined in any coordinate system. However, we choose to define them in the transducer's coordinate system, T , so that calibration parameters (\vec{U} , \vec{V} and k) remain constant for each pose of the transducer.

Because plane parameters are measured in the reference coordinate system, we need to transform them into the transducer's coordinate system for each pose, i ,

$$\vec{n}_i = ({}^T R_R)_i \vec{n}_r, \quad (7)$$

where $({}^T R_R)_i$ is the rotation part of the transducer-to-reference transformation for pose i , $({}^T T_R)_i$, measured by the tracker. After calculating \vec{n}_i is for all p poses and substituting in (6), we can put them in matrix format:

$$\begin{bmatrix} \vec{n}_1^t & m_1 \vec{n}_1^t \\ \vdots & \vdots \\ \vec{n}_p^t & m_p \vec{n}_p^t \end{bmatrix}_{p \times 6} \begin{bmatrix} \vec{U} \\ k \vec{V} \end{bmatrix} = [\vec{0}]_{p \times 1}. \quad (8)$$

The null space of the above matrix gives the solution for $\vec{X}^t = [\vec{U}^t, k \vec{V}^t]$. To obtain the unique solution, \vec{X} is divided by the norm of its first three elements, because \vec{U} is a unit vector:

$$\vec{X}_n = \frac{\vec{X}}{\|\vec{X}(1, 2, 3)\|}. \quad (9)$$

Finally \vec{U} , \vec{V} and k can be easily found:

$$\vec{U} = \vec{X}_n(1, 2, 3), \quad (10)$$

$$\vec{V} = \frac{\vec{X}_n(4, 5, 6)}{\|\vec{X}_n(4, 5, 6)\|}, \quad (11)$$

$$k = \|\vec{X}_n(4, 5, 6)\|. \quad (12)$$

Now the rotation part of ${}^T T_1$ can be determined as

$$R = [\vec{U}_{3 \times 1} \quad \vec{Y}_{3 \times 1} \quad \vec{Z}_{3 \times 1}], \quad (13)$$

$$\vec{Z} = \frac{\vec{U} \times \vec{V}}{\|\vec{U} \times \vec{V}\|}, \quad (14)$$

$$\vec{Y} = \frac{\vec{Z} \times \vec{U}}{\|\vec{Z} \times \vec{U}\|}. \quad (15)$$

In the case of ultrasound beam steering, \vec{U} and \vec{V} are not orthogonal, and the deviation of their crossing angle from 90° can be expressed as the skew angle. Note that here we have calculated k , which is the ratio of axial to lateral pixel-to-millimeter ratios. Therefore, assuming either s_l or s_a is known, the other can be calculated. We use a known s_l based on the number of scan lines across the lateral extent of the transducer array.

The translation part of ${}^T T_1$ is defined by P_0 and can be calculated using (1) by imposing the plane equation:

$$(P_0 + s_l x_i \vec{U} + s_a y_i \vec{V} - Q_i) \cdot \vec{n}_i = 0, \quad (16)$$

where (x_i, y_i) is the location of one point residing on the intersection line in image i . The plane intercept, d , is a known constant for any defined coordinate system:

$$d = Q_r \cdot \vec{n}_r = Q_i \cdot \vec{n}_i, \quad \forall i. \quad (17)$$

Now, (16) can be written in matrix form

$$\begin{bmatrix} \vec{n}_1^t \\ \vdots \\ \vec{n}_p^t \end{bmatrix} P_0 = \begin{bmatrix} d - s_l x_1 \vec{U} \cdot \vec{n}_1 - s_a y_1 \vec{V} \cdot \vec{n}_1 \\ \vdots \\ d - s_l x_p \vec{U} \cdot \vec{n}_p - s_a y_p \vec{V} \cdot \vec{n}_p \end{bmatrix}, \quad (18)$$

which is a linear system of equations and can be solved when at least three non-collinear points are available ($p \geq 3$).

If we assume that the plane equation is unknown and should be solved, the problem can still be solved with a closed-form solution. The Appendix contains the complete derivations of the solution for such problem. It should be noted that more unknowns make the problem less robust and more sensitive to measurement errors.

After the slope of the line is measured using the differential measurement technique, the line equation requires only one more variable (*i.e.*, the line intercept) to be defined. This means that for each image, only one independent equation as in (16) can be written, and other points on the line yield dependent equations. In fact, in (18), the number of independent equations is equal to the number of poses.

Curvilinear transducer calibration

Calibration of a curvilinear transducer is similar to that of a linear transducer except that, if using RF data, a different approach is needed for slope measurement based on the specific geometry of a curvilinear transducer. However, if using scan-converted B-mode data, the plane appears as a straight line, and hence the same method used for a linear transducer can be employed. Next, the differential slope measurement for a curvilinear transducer using RF data is described.

In a curvilinear transducer, the elements are placed with equal spacing on an arc with a certain radius, r_0 . The elements are orientated to follow the arc curvature, resulting in the radial propagation direction, \vec{W} . Here we define \vec{V} as the axial direction corresponding to one of the scan lines (*e.g.*, the middle one), and \vec{U} is a vector perpendicular to \vec{V} in the imaging plane (Fig. 4).

The direction of each scan line, \vec{W}_i , can be described as a linear combination of \vec{U} and \vec{V} , and in terms of q_i , the angle between \vec{U} and \vec{W}_i , as

$$\vec{W}_i = \sin(\theta_i) \vec{U} + \cos(\theta_i) \vec{V}, \quad (19)$$

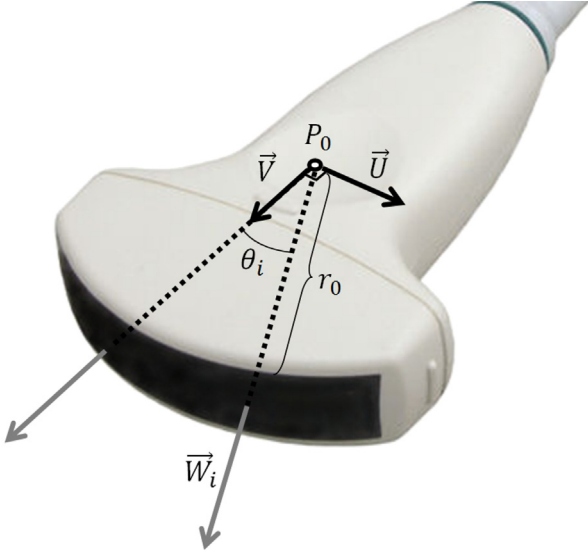


Fig. 4. Elements of a curvilinear transducer are placed on an arc with radius r_0 . The axial direction vector, \vec{W}_i , can be defined in terms of a pair of perpendicular vectors, \vec{U} and \vec{V} .

where q_i is known by the transducer specifications, and therefore, the following coefficients are known:

$$\alpha_i = \sin(\theta_i), \quad \beta_i = \cos(\theta_i). \quad (20)$$

If defining the center of the arc as P_0 , then the position of any point at depth h_i along i th scan line can be described in three dimensions as

$$P = P_0 + (r_0 + s_a h_i) \vec{W}_i, \quad (21)$$

where s_a is the axial pixel-to-millimeter ratio. By combining (19), (20) and (21), while imposing the plane equation for p , we have

$$P_0 \cdot \vec{n} + (r_0 + s_a h_i)(\alpha_i \vec{U} + \beta_i \vec{V}) \cdot \vec{n} = d, \quad (22)$$

where $d = Q \cdot \vec{n}$ and h_i can be calculated as

$$h_i = \frac{d - P_0 \cdot \vec{n}}{s_a \vec{V} \cdot \vec{n}} \frac{1}{\alpha_i m + \beta_i} - \frac{r_0}{s_a}, \quad (23)$$

where $m = \frac{\vec{U} \cdot \vec{n}}{\vec{V} \cdot \vec{n}}$ is in fact the slope of the line, similar to the slope definition in a linear transducer. By writing the same equation for the j th scan line and subtracting it from (23), we have

$$\Delta h = h_i - h_j = e \left(\frac{1}{\alpha_i m + \beta_i} - \frac{1}{\alpha_j m + \beta_j} \right), \quad (24)$$

where e is defined as

$$e = \frac{d - P_0 \cdot \vec{n}}{s_a \vec{V} \cdot \vec{n}}. \quad (25)$$

In (24), Δh comes from the differential measurement, and m and e are the only unknowns. The number of scan lines used to solve (24) varies for each image depending on the number of acceptable scan lines in the segmentation procedure described in the next section. Using (24) for each pair of scan lines, we can solve for the two unknowns (m and e) by minimizing f in the equation below using the Levenberg–Marquardt algorithm (Moré 1978):

$$\sum_{i=1}^{n_{sl}} f = \left[\Delta h_{ij} - e \left(\frac{1}{\alpha_i m + \beta_i} - \frac{1}{\alpha_j m + \beta_j} \right) \right]^2, \quad (26)$$

where n_{sl} is the number of valid pairs of scan lines. j , the pair of the scan line i , was chosen as explained in the next section. This equation can be solved by considering at least two pairs of scan lines. Therefore, for each image, the slope of the line was calculated for the RF data. For B-mode data, a procedure similar to that for the linear transducer was used to calculate the line's slope, m . With the slope values, m_i , being known, the calibration matrix can be calculated using (8). In fact, after the slope values were measured, the data for different poses were combined using a method similar to that for the linear transducer.

Next, the translation parameters were solved using line intercepts, similar to a linear transducer.

Automatic segmentation and measurement

When imaging a flat surface with ultrasound, the RF echo in each scan line is produced at a certain depth of the image. All of these reflection points reside on a straight line, which is the intersection of the imaging plane and the surface (Fig. 3). As long as the echo signatures of at least two scan lines are similar, the slope of this line can be measured very accurately by finding their axial shift with the normalized cross-correlation technique (Walker and Trahey 1995).

Segmentation of the line feature in the ultrasound image is performed as follows. First, in each scan line, the location of the maximum was found and stored in an array as an approximate of the line. To perform differential measurement for more accurate slope estimation, first the image was processed to remove noises, especially reverberation below the actual surface. For this reason, in each scan line, the points around the maximum's location were kept, and the rest of the signal was cleared. Marginal scan lines in both the left and right sides of the image were omitted because they have smaller aperture beam formation and typically greater signal fallout.

At this stage, starting from the left, each scan line was compared against a scan line at a specified lateral distance. A higher lateral distance between the two scan lines is desirable to minimize the sensitivity of slope

estimation to axial measurement error. However, when the two scan lines are too far apart, the pulse shape may change slightly. In our experiments, the distance was chosen as 15 scan lines within an RF image of 128 scan lines.

Each scan line was upsampled by a factor of 10, and the axial shift difference was calculated using the normalized cross-correlation technique. The slope was calculated by dividing this value by the lateral distance times 10. Then, the outlier pairs (CC values < 0.9) were removed, and the average was taken (Fig. 5).

For the curvilinear transducer, first, part of the image that included the scan line that contained strong echoes from the wall was identified. For this reason, the scan line with the highest peak value was identified as the center of the line segment. The line segment was found by starting from this center scan line and adding each scan line at the left or right only if that column's peak value was more than 50% of the highest value. Then, similar to the linear transducer, starting from the left of the left of the image, each scan line was compared against a scan line at a specified lateral distance. Here, the distance was chosen as 10 scan lines.

Plane localization with stylus

In the pre-determined wall method, the plane equation for the wall surface should be determined before the experiment. For this reason, a minimum of three points should be acquired by touching the plane with the stylus. The NDI four-marker probe was used as the stylus, and the plane was traced in a rectangular motion approximately 10×10 cm in size. At the frame rate of 100 fps, 3000 points were collected in 30 s. Although three points are enough for plane localization, acquisition of more points

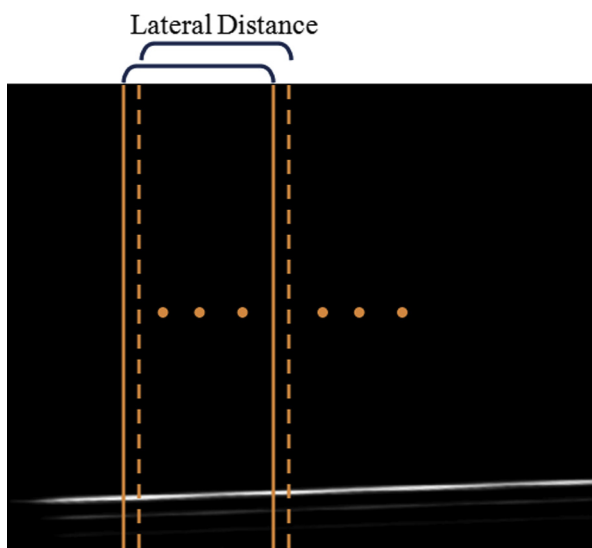


Fig. 5. Each scan line was compared against a scan line at a specified lateral distance (15 scan lines), and the axial shift was calculated using normalized cross-correlation.

in a wide range is suggested to improve accuracy. The plane fitting error was 0.14 mm in our experiment.

To evaluate the accuracy of the stylus, a planar sheet was created with a 3-D printer (Objet, Billerica, MA, USA) comprising a grid of 3×4 semispherical holes on its surface with 30-mm spacing in both directions (Fig. 6). With the stylus, the distances between the holes were measured. The holes were the same size as the stylus bead to make sure it remains fixed at each point. The stylus was positioned with a range of angles (up to 30° tilt angle) during this experiment.

Calibration accuracy evaluation

The point reconstruction accuracy (PRA) test is an objective measure of accuracy where a point is scanned and its location reconstructed in 3-D space using the calculated calibration matrix (Hsu et al. 2008a). The true 3-D location of the point phantom is determined by a tracked stylus. It should be noted that PRA includes all the errors in the tracking and imaging process such as alignment, segmentation, calibration and tracking errors.

To facilitate the validation procedure and acquire multiple points per image, a phantom comprising an array of five truncated cones (top radius = 0.13 mm, bottom radius = 4 mm, height = 15 mm) was manufactured with a 3-D printer. The phantom was fixed at the bottom of the water bath, and its pose was determined by scanning all four semispherical holes incorporated into it with a stylus (alternatively, a rigid body marker could be attached to this phantom). Therefore, the locations of the tops of the cones were always known in the reference coordinate system. A supporting bar (height = 20 mm) resides on each side of the phantom to prevent the transducer from hitting the cone tips and damaging them (Fig. 7a).

The phantom was then scanned by the transducer that was being tracked. The transducer was moved gradually (using a linear stage) in the axial direction 0.5 mm at a time, acquiring 370 points with the linear transducer and 400 points with the curvilinear transducer over a depth range of approximately 40 mm. The tips of the cones in the ultrasound image (Fig. 7b) were kept in the imaging plane by observation of the bright echoes and then segmented manually.

EXPERIMENTS AND RESULTS

The calibration procedure was performed on both linear and curvilinear transducers. One hundred B-mode and RF images of a plane in a water bath were captured for different poses of the transducer. In each pose, the transducer was fixed with a mechanical arm while acquiring the ultrasound image and capturing the

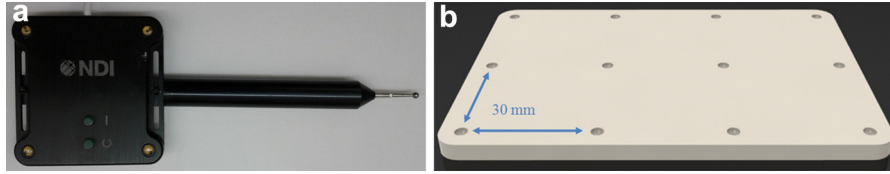


Fig. 6. (a) Stylus being used for plane localization. (b) Phantom with 3×4 semispherical holes for stylus accuracy evaluation.

tracking information. For all images, the imaging depths for the linear and curvilinear transducers were set to 4 and 5 cm, respectively. The transducer was positioned in different poses according to the guidelines given in [Prager et al. \(1998\)](#), who describe the minimal sequence of motions for the single-wall calibration. An attempt was made to maximize the range of translations and rotations while ensuring clear visibility of the line in the ultrasound images. Maximizing the range of translations and rotations ensures that the matrix in (8) is well conditioned and reduces the number of images required to achieve the same level of accuracy.

For comparison, both the linear and curvilinear transducers were also calibrated with a triple N-wire phantom ([Chen et al. 2009](#)) using the f-cal application in the PLUS library ([Lasso et al. 2012](#)).

The PRA is calculated for the proposed method and the N-wire method. Also, evaluation of the accuracy of the stylus and the slope measurement procedure is discussed in this section.

Stylus accuracy

The stylus was pre-calibrated by the manufacturer, but was also calibrated by the pivot procedure in the NDI software. The reported accuracy was 0.15-mm 3-D RMS error and 0.1-mm mean error. To confirm the results, the distances between pairs of points in a 3×4 grid with 30-mm spacing were measured. In a total of

17 measurements between adjacent points in both directions, the error was 0.07 ± 0.13 mm.

Slope measurement evaluation

As mentioned before, to measure the slopes in the differential paradigm, each scan line was compared against a scan line at a specified lateral distance, and the axial shift was measured with the normalized cross-correlation technique. In each image, the average of the CC values is calculated, and the box plots of the average CC values for both RF and B-mode data sets when using linear and curvilinear transducers are provided in [Figure 8](#). The large CC values suggest that echo pulse shape is relatively unchanged among scan lines. These results indicate that CC values for the curvilinear transducer are lower than those for the linear transducer.

Calibration results

We investigated, in particular, the estimation of calibration parameters using different numbers of images. For this reason, the calibration parameters were calculated using different numbers of images, n_s . For each n_s , varying from 20 to 95, n_s images were randomly selected from the data set. The calibration parameters were calculated, and this was repeated 250 times. The average and standard deviation of these calibration parameters were calculated and are illustrated in [Figure 9](#).

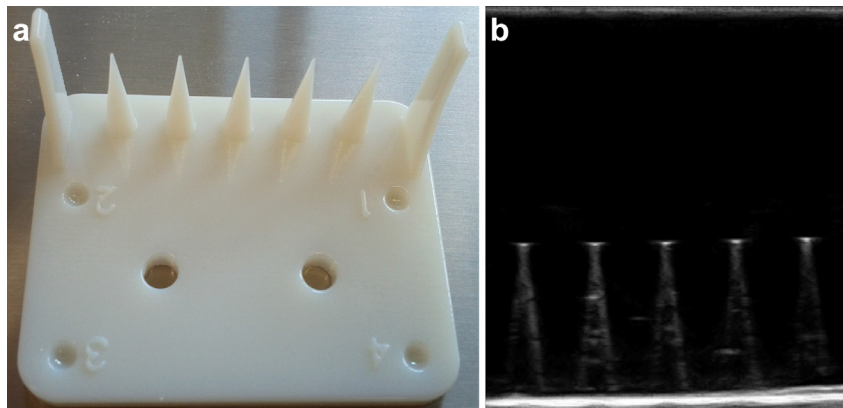


Fig. 7. (a) Point reconstruction accuracy evaluation phantom comprising an array of five truncated cones. (b) Ultrasound image of the point reconstruction accuracy phantom by the linear transducer.

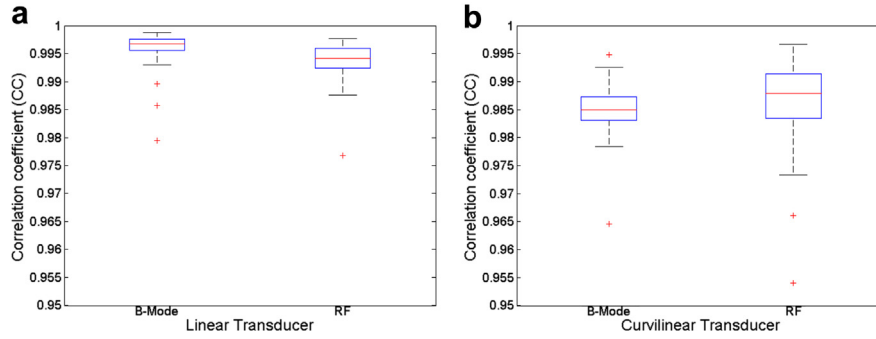


Fig. 8. Box plots of the average correlation coefficient values for all ultrasound images (radiofrequency [RF] and B-mode) for (a) the linear transducer and (b) the curvilinear transducer.

The pre-determined wall method was used on the RF images of the linear transducer. Note that given the closed-form nature of the solution, the order of the images is unimportant. The rotation matrix was decomposed into yaw, pitch and roll angles (α , β , γ) as

$$R = R_z(\alpha)R_y(\beta)R_x(\gamma). \quad (27)$$

Figure 9 illustrates that the standard deviation of the parameters rapidly decreases as the number of input images increases, with diminishing returns after 100

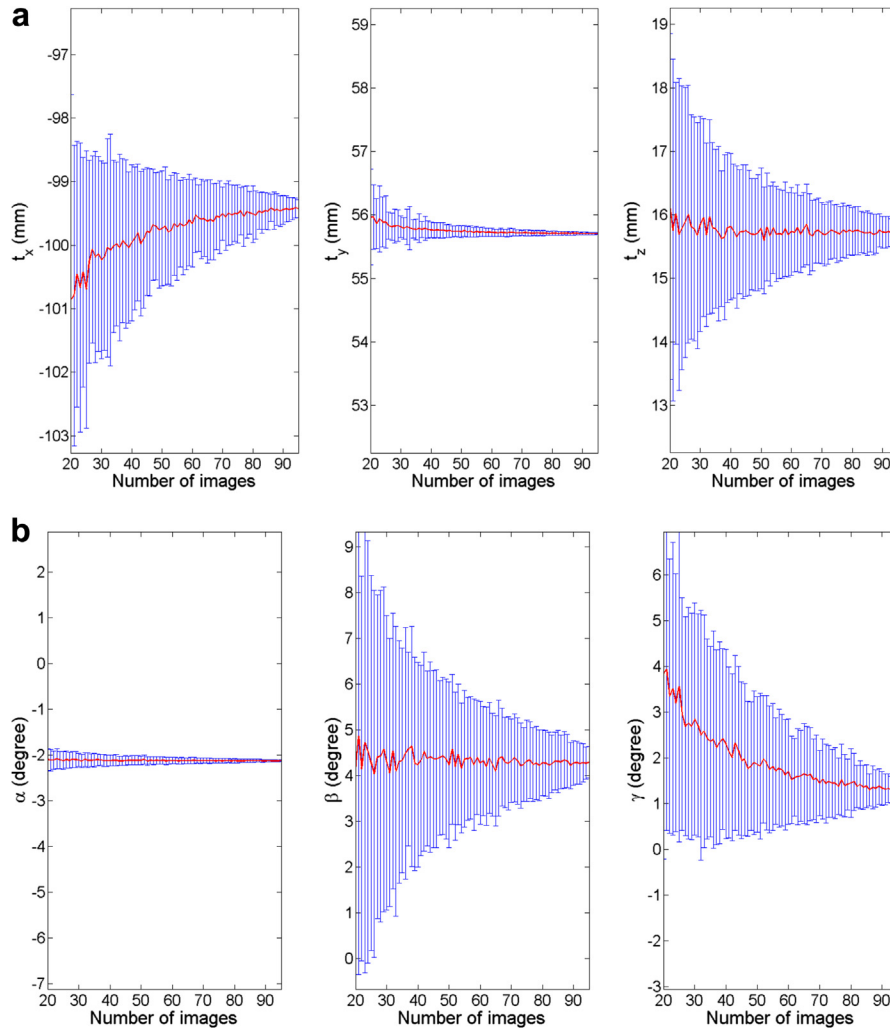


Fig. 9. Calibration results for the pre-determined single-wall method using 20 to 95 radiofrequency images of the linear transducer. Means (red) and standard deviations (blue) of the calibration parameters are calculated: (a) translation parameters (t_x , t_y , t_z) (mm), (b) rotation parameters (α , β , γ) (degrees).

images. Also, it indicates that out-of-plane rotation parameters (β and γ) are estimated with less precision than is in-plane rotation (α). The reason is that the image features (line slopes) are less sensitive to out-of-plane rotations. This is an inevitable effect of a 2-D imaging modality and affects other 2-D calibration methods as well (e.g., Figure 11 in Chen *et al.* 2009).

In a similar fashion, calibration results for the curvilinear transducer were calculated and are illustrated in Figure 10.

Calibration accuracy

The accuracy of the proposed calibration methods was evaluated and compared with that of the N-wire method for both linear and curvilinear transducers. As described earlier, 370 and 400 points were acquired by the linear and curvilinear transducers, respectively, over

a depth range of approximately 40 mm. The locations of the segmented points in the images were compared with the estimated positions of the cone tips on each image plane, and the Euclidean distance error was measured. Tables 1 and 2 summarize the results for the linear and curvilinear transducers, respectively. Moreover, the mean and standard deviation of PRA as a function of number of images were calculated using the same frame-selection method as described in the preceding section. The result is illustrated in Figure 11.

Calibration time

Localization of the plane takes 30 s, as mentioned earlier. The image acquisition time is proportional to the number of images. In our experiments, acquisition of 100 different images took about 5 min. With our closed-form solution, the processing time for calculation

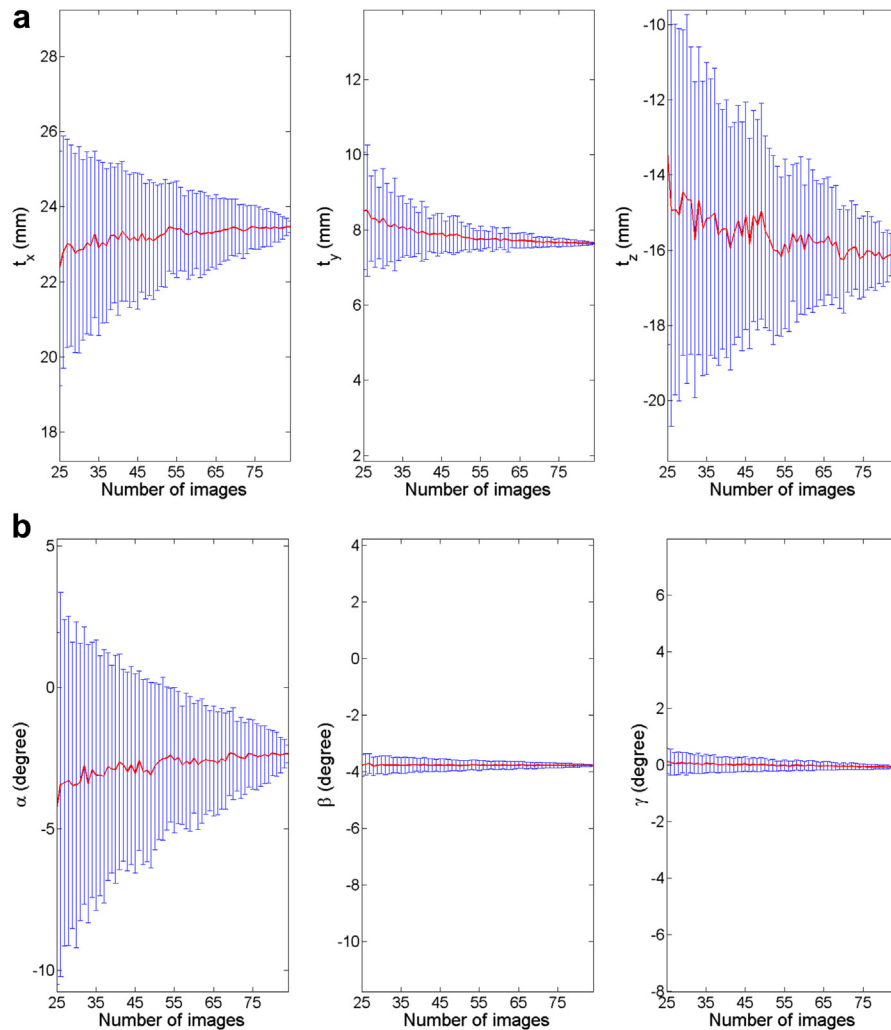


Fig. 10. Calibration results for the pre-determined single-wall method using 25 to 80 radiofrequency images of the curvilinear transducer. Means (red) and standard deviations (blue) of the calibration parameters are calculated: (a) translation parameters (t_x, t_y, t_z) (mm), (b) rotation parameters (α, β, γ) (degrees).

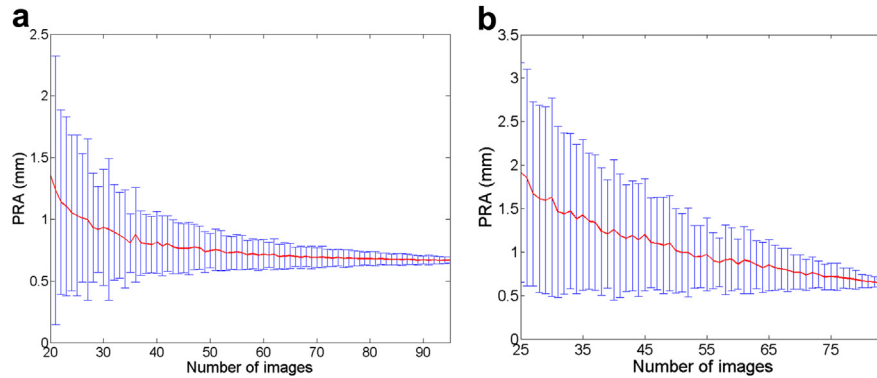


Fig. 11. Means (red) and standard deviations (blue) of point reconstruction accuracy (PRA) values using different numbers of radiofrequency images: (a) linear transducer, (b) curvilinear transducer.

of the calibration results takes only a few seconds on a standard computer workstation with a Core 2 Duo CPU at 2.93 GHz and 4 GB of RAM.

DISCUSSION AND CONCLUSIONS

Although there are many calibration methods, including recently introduced methods using differential measurements on multiple wedges (Najafi et al. 2014), there is still a need for a simple and accurate calibration method. The single-wall method (Prager et al. 1998) is an obvious choice to consider in extending the differential calibration method to improve ease-of-use. The original single-wall method uses an iterative solver to find the calibration parameters as well as the plane equation. According to Prager et al. (1998), the single-wall phantom produced slightly ill-conditioned sets of calibration equations because of the limited range of scanning motions that resulted in clear images of the wall.

In this article, we propose an improved single-wall calibration for both linear and curvilinear transducers and for both RF and B-mode input data. The key is to adapt the differential measurement approach to a single wall. We also propose to simplify the calibration problem by explicitly measuring the position of the plane using a stylus and, thus, reduce the number of unknowns and formulate a closed-form solution. The goal was to obtain good accuracy with a relatively small number of images. The PRA evaluation was performed comparing 370 and 400 points for linear and curvilinear transducers, respec-

tively, throughout the image to their estimated projections using the method and the triple N-wire method. The pre-determined wall method, for the linear transducer, achieves a PRA of 0.73 ± 0.23 using 100 RF images, whereas the triple N-wire PRA was 0.67 ± 0.20 mm using 100 B-mode images. For the curvilinear transducer, the PRA of the pre-determined method was 0.86 ± 0.28 using 100 RF images, whereas the PRA of the triple N-wire method using the same number of B-mode images was 0.80 ± 0.46 mm. All the methods statistically significantly differed, with p -values < 0.05 .

Similar to the inherent limitations of the single-wall method, in our generalized closed-form solution (Appendix), we observed that the method is sensitive to measurement and tracking errors. The PRA for the generalized (without pre-determination of wall position) is 3.81 ± 0.87 mm for RF data and 5.16 ± 0.49 for B-mode data for the linear transducer, and 3.88 ± 0.51 mm for RF data and 4.08 ± 1.21 mm for B-mode data for the curvilinear transducer. These are clearly inferior to values for the pre-determined method. Although, in the first stage, the errors in estimation of rotation parameters and plane normal are reasonable, these errors largely affect estimation of the plane intercept and translation parameters.

The traditional single-wall method was implemented in MATLAB (The MathWorks, Natick, MA, USA) using the same algorithm as in Prager et al. (1998), and it was applied to the same B-mode data in our experiments. PRAs of 3.12 ± 1.01 mm and 4.03 ± 1.51 mm were achieved for linear and curvilinear

Table 1. Calibration point reconstruction accuracy test results for the linear transducer

	Top (4–15 mm)	Center (15–26 mm)	Bottom (26–37 mm)	Total (4–37 mm)
Number of points	130	127	113	370
Pre-determined radiofrequency	0.66 ± 0.22	0.68 ± 0.20	0.76 ± 0.17	0.73 ± 0.23
Pre-determined B-mode	1.75 ± 0.25	1.41 ± 0.22	1.15 ± 0.20	1.49 ± 0.40
N-Wire B-mode	0.65 ± 0.21	0.65 ± 0.20	0.64 ± 0.16	0.67 ± 0.20

Table 2. Calibration point reconstruction accuracy test results for the curvilinear transducer

	Top (12–23 mm)	Center (23–35 mm)	Bottom (35–46 mm)	Total (12–46 mm)
Number of points	117	130	153	400
Predetermined radiofrequency	0.61 ± 0.20	0.82 ± 0.23	0.99 ± 0.21	0.86 ± 0.28
Predetermined B-mode	1.41 ± 0.20	1.18 ± 0.23	1.34 ± 0.22	1.33 ± 0.27
N-Wire B-mode	0.53 ± 0.33	0.76 ± 0.38	0.80 ± 0.33	0.80 ± 0.46

transducers, respectively. Note that [Prager et al. \(1998\)](#) reported that the traditional single-wall method was found to produce a mean and maximum of the point reconstruction precision of 3.43 and 11.67 mm, respectively. In implementation of the traditional single-wall method by ([Hsu et al. 2009](#)), a PRA of 2.28 mm was reported using B-mode data of a linear transducer with an imaging depth of 3 cm.

In terms of calibration time, our automatic image processing algorithm runs at the ultrasound frame rate, and the final results are calculated in a few seconds thanks to our proposed closed-form solution. We used a relatively small number of images (*i.e.*, 100) to reduce calibration time, compared with the 480 and 530 images used in the traditional single wall and Cambridge phantom, respectively ([Prager et al. 1998](#)). The N-wire method also uses 100 images for calibration ([Chen et al. 2009](#)). Calibration time is important if, for example, the calibration must be done repetitively in an operating room ([Kowal et al. 2003](#)).

The pre-determined wall method requires that the plane be localized (using a stylus) before calibration, but increases the accuracy and robustness of the solution to a great extent. This can either be done with a stylus before each calibration, or once and thereafter known by affixing a tracker permanently to the wall.

The proposed method is less accurate compared with the multiwedge phantom ([Najafi et al. 2014](#)) with PRAa of 0.18 ± 0.40 and 0.09 ± 0.39 mm for B-mode and RF data, respectively. This is to be expected because there are five optimized plane locations using that phantom, which obviously has the drawback of requiring a specialized phantom. We therefore see the proposed differential pre-determined single-wall calibration approach as complementary to the multiwedge approach.

Note that direct comparison of errors between calibration methods in different articles should be done with caution because different apparatus and parameters were used. It should also be noted that PRA tests, like other measures of calibration, include errors in distinguishing the point target location within the image, which affects the ability of a point to act as a “gold standard.” Such concerns about the gold standard are analogous to the concerns about choosing appropriate image features for calibration; that is, at the sub-millimeter level, it is

difficult to separate calibration errors from errors in the gold standard.

It is worth mentioning that in a PRA test, the key is to place the point target in the ultrasound image plane with the highest accuracy possible. The position of the stylus (or the transducer), on the other hand, does not affect the accuracy of the PRA test, assuming uniform tracking accuracy of the tracker. In fact, the PRA test is most meaningful when many target points are placed throughout the image, with the highest accuracy possible in aligning the points with the ultrasound image plane. Obviously, the goal is to minimize the alignment error, but zero alignment error might not be possible. The proposed PRA phantom reduces the alignment error with its cone-shaped target points. It also increases the speed by a factor of 5, facilitating acquisition of more points across the image in a timely manner.

It is worth mentioning that in a curvilinear transducer, not all the scan lines produce a strong echo reflection because of the curvature of the transducer. However, the upside is that because of the curvature of the transducer, a larger range for in-plane rotations is possible compared with a linear transducer.

The differential measurement improves the accuracy of line slope measurement; however, there are issues that limit its effect in the generalized method in achieving high accuracy. One issue is the sensitivity of the proposed closed-form solution (*i.e.*, generalized method) to slope measurement error. The reason is that in the closed-form solution, the calibration parameters are calculated in two stages (*i.e.*, null space and Kronecker decomposition) and are not calculated directly. Another issue is that the rotation parameters and the plane normal are calculated first, and then the translation and plane intercept are calculated. Because of the specific mathematical formulation of the problem and its sensitivity, as mentioned earlier, the rotational parameters cannot be calculated with very high accuracy. This, in turn, results in inaccuracies in estimation of the translation parameters and the plane intercept. In the traditional single wall, on the other hand, all the parameters are solved at the same time, and the translational parameters, in a way, act as a regularization term in the iterative solution.

In fact, because the two methods have different mathematical bases, it is not possible to solely compare

the effect of the differential measurement technique. However, the mathematical formulation of the pre-determined method allows the use of differential measurements and takes advantage of higher measurement accuracy while providing a direct and robust solution for calibration parameters.

We are currently integrating the software into the PLUS library (Lasso et al. 2012) so it is freely available to other researchers.

Although a transformation such as beam steering will not produce a different pose, it can be used to increase the range of motion by allowing wider range of rotations for the transducer when applied in the opposite direction of rotation to improve the image quality. Future work includes investigating this technique to improve the performance of the method.

The method can be extended to calibration of 3-D ultrasound transducers by considering that the axial difference of two scan lines at different elevations (*i.e.*, in different frames) yields a new equation similar to (1). This is equivalent to measuring the slope of a line in a re-sliced plane of the acquired volume. This extra equation reduces the number of required images and improves the accuracy. This is under the assumption of equal spacing between the frames. Otherwise, the calibration can be performed on every single frame of the volume, similar to a 2-D transducer. That is also part of our future research.

Acknowledgments—This work is supported by the Natural Sciences and Engineering Research Council of Canada and the Canadian Institutes of Health Research.

REFERENCES

- Amin DV, Kanade T, Jaramaz B, DiGioia AM III, Nikou C, LaBarca RS, Moody JE Jr. Calibration method for determining the physical location of the ultrasound image plane. In: Wiro J, Viergever Niessen Max A, (eds). *Medical Image Computing and Computer-Assisted Intervention—MICCAI 2001*. Berlin/Heidelberg: Springer; 2001. p. 940–947.
- Bergmeir C, Seitel M, Frank C, Simone R, Meinzer H, Wolf I. Comparing calibration approaches for 3-D ultrasound probes. *Int J Comput Assist Radiol Surg* 2009;4:203–213.
- Blackall J, Rueckert D, Maurer CRJ, Penney G, Hill D, Hawkes D. An image registration approach to automated calibration for freehand 3 D ultrasound. In: . Berlin/Heidelberg: Springer; 2000. p. 462–471.
- Bocor E, Viswanathan A, Choti M, Taylor RH, Fichtinger G, Hager G. A novel closed form solution for ultrasound calibration. *Proc IEEE Int Symp Biomed Imaging: Nano to Macro* 2004;1:527–530.
- Bocor EM, Iordachita I, Fichtinger G, Hager GD. Ultrasound self-calibration. *Proc SPIE* 2006;6141:61412.
- Brendel B, Winter S, Ermert H. A simple and accurate calibration method for 3-D freehand ultrasound. *Biomed Technik* 2004;49: 872–873.
- Chen TK, Thurston AD, Ellis RE, Abolmaesumi P. A real-time freehand ultrasound calibration system with automatic accuracy feedback and control. *Ultrasound Med Biol* 2009;35:79–93.
- Chinnaiyan P, Tomee W, Patel R, Chappell R, Ritter M. 3-D-ultrasound guided radiation therapy in the post-prostatectomy setting. *Technol Cancer Res Treat* 2003;2:455.
- Cosio F, Lira Berra E, Montiel N, Segundo C, Garduo E, Gonzalez M, Quispe Siccha R, Ramirez B, Hazan Lasri E. Computer assisted biopsy of breast tumors. *Conf Proc IEEE Eng Med Biol Soc* 2010; 2010:5995–5998.
- Detmer PR, Bashein G, Hodges T, Beach KW, Filer EP, Burns DH, Strandness DE. 3-D ultrasonic image feature localization based on magnetic scanhead tracking: *In vitro* calibration and validation. *Ultrasound Med Biol* 1994;20:923–936.
- Eggert D, Lorusso A, Fisher R. Estimating 3-D rigid body transformations: A comparison of four major algorithms. *Mach Vision Appl* 1997;9:272–290.
- Gee AH, Houghton NE, Treece GM, Prager RW. A mechanical instrument for 3-D ultrasound probe calibration. *Ultrasound Med Biol* 2005;31:505–518.
- Genton MG. Separable approximations of space-time covariance matrices. *Environmetrics* 2007;18:681–695.
- Gulati S, Berntsen EM, Solheim O, Kvistad KA, Hberg A, Selbekk T, Torp SH, Unsgaard G. Surgical resection of high-grade gliomas in eloquent regions guided by blood oxygenation level dependent functional magnetic resonance imaging, diffusion tensor tractography, and intra-operative navigated 3-D ultrasound. *Minim Invasive Neurosurg* 2009;52:17–24.
- Hsu P, Prager R, Gee A, Treece G, Sensen C, Hallgrmsson B. Freehand 3-D ultrasound calibration: A review. *Adv Imaging Biol Med* 2009;47–84.
- Hsu P, Treece G, Prager R, Houghton N, Gee A. Comparison of freehand 3-D ultrasound calibration techniques using a stylus. *Ultrasound Med Biol* 2008a;34:1610–1621.
- Hsu PW, Prager RW, Gee AH, Treece GM. Real-time freehand 3 d ultrasound calibration. *Ultrasound Med Biol* 2008b;34:239–251.
- Huang X, Gutiérrez L, Stanton D, Kim P, Jain A. Image registration based 3-D TEE-EM calibration. *Proc IEEE Int Conf Biomed Imaging: From Nano to Macro* 2010;1209–1212.
- Khamene A, Sauer F. A novel phantom-less spatial and temporal ultrasound calibration method. In: . Berlin/Heidelberg: Springer; 2005. p. 65–72.
- Kowal J, Amstutz CA, Caversaccio M, Nolte LP. On the development and comparative evaluation of an ultrasound B-mode probe calibration method. *Comput Aided Surg* 2003;8:107–119.
- Krekel N, Zonderhuis B, Schreurs H, Cardozo A, Rijna H, van der Veen H, Muller S, Poortman P, de Widt L, de Roos W, Bosch AM, Taets van Amerongen AHM, Bergers E, van der Linden M, de Lange de Klerk ESM, Winters HAH, Meijer S, van den Tol PMP. Ultrasound-guided breast-sparing surgery to improve cosmetic outcomes and quality of life. a prospective multicentre randomised controlled clinical trial comparing ultrasound-guided surgery to traditional palpation-guided surgery (COBALT trial). *BMC Surg* 2011;11:8.
- Lange T, Kraft S, Eulenstein S, Lamecker H, Schlag P. Automatic calibration of 3-D ultrasound probes. *Bildverarbeitung Med* 2011;2011: 169–173.
- Lasso A, Heffter T, Pinter C, Ungi T, Fichtinger G. Implementation of the PLUS open-source toolkit for translational research of ultrasound-guided intervention systems. In: *Medical Image Computing and Computer-Assisted Intervention—MICCAI 2012: Systems and Architectures for Computer Assisted Interventions*. MIDAS J 2012;1–12.
- Lindseth F, Lang T, Bang J, Nagelhus Hernes TA. Accuracy evaluation of a 3-D ultrasound-based neuronavigation system. *Comput Aided Surg* 2002;7:197–222.
- Lindseth F, Tangen GA, Langø T, Bang J. Probe calibration for freehand 3-D ultrasound. *Ultrasound Med Biol* 2003;29:1607–1623.
- Loan C.V. and Pitsianis N., Approximation with Kronecker products. Technical report, 1992, Linear Algebra for Large Scale and Real-Time Applications NATO ASI Series Volume 232, 1993, pp 293–314 Cornell University.
- Melvær E, Mørken K, Samset E. A motion constrained cross-wire phantom for tracked 2-D ultrasound calibration. *Int J Comput Assist Radiol Surg* 2012;7:611–620.
- Mercier L, Lang T, Lindseth F, Collins DL. A review of calibration techniques for freehand 3-D ultrasound systems. *Ultrasound Med Biol* 2005;31:449–471.

- Moré JJ. In: The Levenberg–Marquardt algorithm: Implementation and theory. In: Numerical analysis. Berlin/Heidelberg: Springer; 1978. p. 105–116.
- Muratore DM, Galloway RL. Beam calibration without a phantom for creating a 3-D freehand ultrasound system. *Ultrasound Med Biol* 2001;27:1557–1566.
- Najafi M, Afsham N, Abolmaesumi P, Rohling R. A closed-form differential formulation for ultrasound spatial calibration. In: . p. 44–53. Berlin/Heidelberg: Heidelberg.
- Najafi M, Afsham N, Abolmaesumi P, Rohling R. Single wall closed-form differential ultrasound calibration. *Proc SPIE* 2012b;8316: 83162A.
- Najafi M, Afsham N, Abolmaesumi P, Rohling R. A closed-form differential formulation for ultrasound spatial calibration: Multi-wedge phantom. *Ultrasound Med Biol* 2014;40:2231–2243.
- Nakamoto M, Nakada K, Sato Y, Konishi K, Hashizume M, Tamura S. Intraoperative magnetic tracker calibration using a magneto-optic hybrid tracker for 3-D ultrasound-based navigation in laparoscopic surgery. *IEEE Trans Med Imaging* 2008;27:255–270.
- Pagoulatos N, Haynor D, Kim Y. A fast calibration method for 3-D tracking of ultrasound images using a spatial localizer. *Ultrasound Med Biol* 2001;27:1219–1229.
- Paulius K, Maguina P, Mejia A. Ultrasound-guided management of hand fractures. *Orthopedics* 2008;31:1204–1207.
- Peterhans M, Anderegg S, Gaillard P, Oliveira-Santos T, Weber S. A fully automatic calibration framework for navigated ultrasound imaging. *Proc IEEE Int Conf Eng Med Biol Soc* 2010;2010: 1242–1245.
- Peters A, Baker R, Sangeux M. Validation of 3-D freehand ultrasound for the determination of the hip joint centre. *Gait Posture* 2010;31: 530–532.
- Prager RW, Gee A, Berman L. Stradx: Real-time acquisition and visualization of freehand three-dimensional ultrasound. *Med Image Anal* 1999;3:129–140.
- Prager RW, Rohling RN, Gee AH, Berman L. Rapid calibration for 3-D freehand ultrasound. *Ultrasound Med Biol* 1998;24:855–869.
- Rouviere O, Souchon R, Salomir R, Gelet A, Chapelon J, Lyonnet D. Transrectal high-intensity focused ultrasound ablation of prostate cancer: Effective treatment requiring accurate imaging. *Eur J Radiol* 2007;63:317–327.
- Trobaugh J, Richard W, Smith K, Bucholz R. Frameless stereotactic ultrasonography: Method and applications. *Comput Med Imaging Graphics* 1994;18:235–246.
- Unsgård G. Ultrasound-guided neurosurgery. Practical handbook of neurosurgery. Berlin/Heidelberg: Springer; 2009. p. 907–926.
- Walker WF, Trahey GE. A fundamental limit on delay estimation using partially correlated speckle signals. *IEEE Trans Ultrason Ferroelectr Freq Control* 1995;42:301–308.
- Yan C, Goulet B, Pelletier J, Chen S, Tampieri D, Collins D. Towards accurate, robust and practical ultrasound-CT registration of vertebrae for image-guided spine surgery. *Int J Comput Assist Radiol Surg* 2011;6:523–537.
- Yaniv Z, Foroughi P, Kang H, Bocktor E. Ultrasound calibration framework for the image-guided surgery toolkit (IGSTK). *Proc SPIE* 2011;7964:79641N.

APPENDIX

In this approach, it is assumed that no prior information about the plane is available and the plane equation is considered unknown and should also be solved. Therefore, the parameters are all defined in the reference coordinate system (instead of transducer coordinate system):

$$\vec{U}_{ri} = ({}^R R_T)_i \vec{U}, \quad (\text{A.1})$$

$$\vec{V}_{ri} = ({}^R R_T)_i \vec{V}. \quad (\text{A.2})$$

The calibration vectors for one transducer pose, (U_{r0}, \vec{V}_{r0}) , are considered as the unknowns, and the corresponding vectors for other poses are defined relative to them:

$$\vec{U}_{ri} = ({}^R R_T)_i ({}^R R_T)_0^{-1} \vec{U}_{r0}, \quad (\text{A.3})$$

$$\vec{V}_{ri} = ({}^R R_T)_i ({}^R R_T)_0^{-1} \vec{V}_{r0}, \quad (\text{A.4})$$

Thus, we can define

$$R_{di} = ({}^R R_T)_i ({}^R R_T)_0^{-1}, \quad (\text{A.5})$$

which is a known matrix obtained from the tracker. And now, by substituting (A.3), (A.4) and (A.5) into (6), we obtain

$$(R_{di} \vec{U}_{r0}) \cdot \vec{n} + k m_i (R_{di} \vec{V}_{r0}) \cdot \vec{n} = 0, \quad (\text{A.6})$$

where \vec{U}_{r0} , \vec{V}_{r0} , n and k are unknowns, and R_{di} and m_i are the known measurements.

To solve (A.6), first we rearrange it so that the dot product is replaced with vector multiplication and then vectorize the two elements:

$$\text{vec}(\vec{n}^t R_{di} \vec{U}_{r0}) + k m_i \text{vec}(\vec{n}^t R_{di} \vec{V}_{r0}) = 0, \quad (\text{A.7})$$

Here, $\text{vec}(X)$ denotes the vectorization of the matrix X formed by stacking the columns of X into a single column vector. Now, using the property of the Kronecker product,

$$\text{vec}(AXB) = (B^t \otimes A) \text{vec}(X), \quad (\text{A.8})$$

we can rewrite (A.8) as

$$(\vec{U}_{r0}^t \otimes \vec{n}^t) \text{vec}(R_{di}) + k m_i (\vec{V}_{r0}^t \otimes \vec{n}^t) \text{vec}(R_{di}) = 0, \quad (\text{A.9})$$

which can be rearranged and put in matrix form as

$$\begin{bmatrix} \text{vec}(R_{d1})^t, m_1 \text{vec}(R_{d1})^t \\ \vdots \\ \text{vec}(R_{dp})^t, m_p \text{vec}(R_{dp})^t \end{bmatrix} \begin{bmatrix} \vec{U}_{r0} \otimes \vec{n} \\ k \vec{V}_{r0} \otimes \vec{n} \end{bmatrix} = 0, \quad (\text{A.10})$$

The null space of the above equation gives the solution, X_g . Similar to (8), the obtained solution should be normalized first to satisfy $\|\vec{U}_{r0} \otimes \vec{n}\| = 1$, and k can also be solved as

$$k = \frac{X_g(10:18)}{\|X_g(10:18)\|}. \quad (\text{A.11})$$

Now \vec{U}_{r0} , \vec{V}_{r0} and \vec{n} should be calculated from X_g :

$$\vec{U}_{r0} \otimes \vec{n} = X_g(1:9), \quad (\text{A.12})$$

$$\vec{V}_{r0} \otimes \vec{n} = \frac{X_g(10:18)}{k}. \quad (\text{A.13})$$

The solution for \vec{U}_{r0} , \vec{V}_{r0} and n can be found using an approximation method with Kronecker products (Genton 2007; Loan and Pitsianis 1992). In this method, the problem is finding the $B_{m_1 \times n_1}$ and $C_{m_2 \times n_2}$ that minimize $\|A - B \otimes C\|_F$, where subscript F denotes the Frobenius norm, and A is an $m \times n$ matrix with $m = m_1 m_2$ and $n = n_1 n_2$.

An appealing solution results from the use of the Frobenius norm; using other norms would lead to a computationally difficult optimization problem (Genton 2007). The solutions are the singular vectors associated with the largest singular value of \hat{A} , a permuted version of A , by singular value decomposition (SVD). If $A = PSQ^t$, then $\text{vec}(A) = \alpha_1 p_1$ and $\text{vec}(B) = \alpha_2 q_1$ and $\alpha_1 \alpha_2 = \alpha_1$.

To apply this method to (A.12) and (A.13), first the right-hand side should be permuted into a 3×3 matrix, and then the singular value decomposition should be computed:

$$H_1 = \begin{bmatrix} X_{g1} & X_{g2} & X_{g3} \\ X_{g4} & X_{g5} & X_{g6} \\ X_{g7} & X_{g8} & X_{g9} \end{bmatrix} = PSQ^t, \quad (\text{A.14})$$

and

$$H_2 = \frac{1}{k} \begin{bmatrix} X_{g10} & X_{g11} & X_{g12} \\ X_{g13} & X_{g14} & X_{g15} \\ X_{g16} & X_{g17} & X_{g18} \end{bmatrix} = P' S' Q', \quad (\text{A.15})$$

Eventually,

$$\vec{U}_{r0} = p_1, \quad (\text{A.16})$$

$$\vec{V}_{r0} = p'_1, \quad (\text{A.17})$$

$$\vec{n} = q_1 = q'_1. \quad (\text{A.18})$$

Note that because of the unity of all the vectors, $\alpha_1 = \alpha_2 = \sigma'_1 = 1$. Then, by use of (A.1) and (A.2), \vec{U} and \vec{V} can be calculated, and eventually, similar to the previous section, the calibration rotation matrix can be computed using (13), (14) and (15).

To solve for the translation part, P_0 , again we use (16) and (17). However, here d is considered as an unknown, and therefore, the matrix form should be reformulated as

$$\begin{bmatrix} \vec{n}_1' - 1 \\ \vdots \\ \vec{n}_p' - 1 \end{bmatrix} \begin{bmatrix} P_0 \\ d \end{bmatrix} = \begin{bmatrix} -s_{lx1} \vec{U} \cdot \vec{n}_1 - s_{dy1} \vec{V} \cdot \vec{n}_1 \\ \vdots \\ -s_{lxp} \vec{U} \cdot \vec{n}_p - s_{dyp} \vec{V} \cdot \vec{n}_p \end{bmatrix}, \quad (\text{A.19})$$

which is also a linear system of equations that requires at least four points ($p \geq 4$) to solve for $[P_0]_{3 \times 1}$ and d .